



Catalysis
Science &
Technology

**Predicting an Optimal Oxide/Metal Catalytic Interface for
Hydrodeoxygenation Chemistry of Biomass Derivatives**

Journal:	<i>Catalysis Science & Technology</i>
Manuscript ID	CY-ART-04-2021-000707.R2
Article Type:	Paper
Date Submitted by the Author:	11-Jul-2021
Complete List of Authors:	Deo, Shyam; Pennsylvania State University, Janik, Michael; Pennsylvania State University, Chemical Engineering

SCHOLARONE™
Manuscripts

Predicting an Optimal Oxide/Metal Catalytic Interface for Hydrodeoxygenation

Chemistry of Biomass Derivatives

Shyam Deo*, Michael J. Janik*¹

*Department of Chemical Engineering, The Pennsylvania State University, University Park, Pennsylvania 16802, United States

¹email: mjj13@psu.edu

Abstract

Complex reaction pathways such as hydrodeoxygenation (HDO) of multi-oxygenated reactants like furfuryl alcohol towards 2-methylfuran can benefit from a close connection between multi-component (oxide-metal) catalytic site properties and their catalytic performance. The HDO activity can be tuned by optimizing the synergy between the individual metal oxide and metal site properties towards the HDO catalytic cycle consisting of C-O activation, C-H formation, and oxygen vacancy formation steps. Through our previously reported model of oxide-metal interface catalyst – a TiO₂ nanorod on a Pd (111) surface, we identified following material descriptors that dictate furfuryl alcohol HDO activity: work function (Φ), oxygen vacancy formation energy (ΔE_{vac}), metal-carbon binding energy ($M\text{-}C_{\text{B.E.}}$), and extent of metal-metal oxide interfacial charge transfer (q). The descriptors were examined over the interface with the composition altered towards closed pack metals: Ag, Au, Cu, Pd, Rh, Ru and Zn, and monolayer surfaces of Ag, Au, Co, Cu, Fe, Ir, Ni, Pt, Rh, Ru and Zn metals atop Pd (111). We identified a greater stabilization of the C-O activation transition state, the key HDO step, through electronic charge redistribution at the interface, facilitated by a higher metal work function. Stronger metal-carbon binding dictates the favorable hydrogenation of the resulting organic fragment. The role of these descriptors was further investigated under experimentally relevant hydrogenation reaction conditions of H₂ and hydrocarbons partial pressures. Such fundamental knowledge of the descriptors dictating HDO can

2

provide opportunities for further tuning the structural, electronic, and chemical properties of a multicomponent interface to achieve optimal HDO activity.

1. Introduction

Metal/metal oxide catalytic interfaces can offer unique activity or selectivity due to the multi-component bifunctionality or emergent chemical properties at the interface. Hydrodeoxygenation (HDO) reactions have been demonstrated to take advantage of these interfacial properties.¹⁻⁹ Redox functionality of the metal oxide aids in breaking the C-O bond, while the metal can facilitate H₂ dissociation and C-H formation.⁷ In addition to bifunctionality, electron transfer between the oxide and the metal alters reactivity, providing emergent chemical properties unique to the interface.^{10, 11} We previously used density functional theory (DFT) calculations¹² to demonstrate how the TiO₂/Pd interface promotes selectivity to HDO, helping to explain experimental observations of enhanced selectivity for TiO₂-coated Pd nanoparticles.¹ In this work, we extend our DFT model of the TiO₂/Pd interface (**Figure 1**), altering the composition of this interface to develop a set of physical and/or electronic descriptors that predict optimal HDO activity at the metal oxide/metal interface.

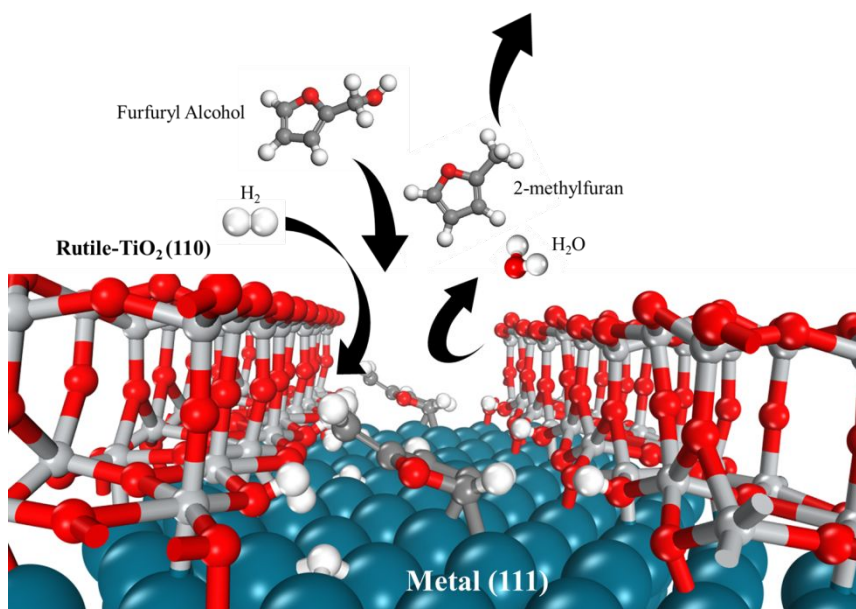


Figure 1. Schematic of hydrodeoxygenation of furfuryl alcohol to 2-methylfuran over an oxide “nanorod”/extended metal surface model for the metal/oxide interface.

Prior DFT and experimental studies have demonstrated the enhanced activity and selectivity of metal/metal oxide interfaces for biomass deoxygenation.^{9, 13, 14} For example, DFT and experimental studies by Omotoso et al. reported an enhancement in the rate of toluene formation from m-cresol over a Ru/TiO₂ catalyst relative to Ru/SiO₂ and explained this enhancement as due to a proton-assisted deoxygenation path over an oxygen vacancy in TiO₂.⁹ The HDO rate increased linearly with the Ru/oxide perimeter, and partially reduced TiO₂ along the perimeter was proposed to provide active sites that lowered the HDO barrier. DFT studies over WO_x-decorated Pt/C catalysts also reported that oxygen vacancy formation was facilitated for a Pt/WO_x film, which favored m-cresol adsorption and direct hydrogenolysis of its C-O bond.³ These studies attributed enhanced HDO to metal/metal oxide interfacial sites, invoking distinct mechanistic roles of the metal and the oxide and their cooperativity towards HDO. Despite success in specific systems, principles for optimizing metal/metal oxide components for optimal interfacial HDO activity remain unclear.

4

Previous DFT studies have collectively demonstrated that metal/metal oxide interfaces provide unique and tunable functionality to facilitate deoxygenation. These multifunctional interfaces provide HDO activities that exceed single component “volcano curve” limitations.^{4, 15} Oxide components can generate reduced active sites, in the presence of H₂, to assist in C–O bond scission of oxygenates,⁷ while metallic sites can bind the resultant unsaturated carbon atoms as well as aromatic rings through ring π -metal d orbital interactions.⁸ Synergistic effects between oxides and metals may also increase the H₂-metal sticking probability.¹⁶ Such delineated roles of the metals and the oxides towards HDO build a framework for identifying physical, chemical and/or electronic descriptors to construct highly active multicomponent catalytic systems. In short, the rationale for interfacial design relies on optimizing material properties of the individual components such that the synergy towards the HDO catalytic cycle is maximized.

Using our previously reported model of oxide-metal interfacial sites represented by rutile nanorod-TiO₂ on a Pd (111) surface,¹² we aim to predict an optimal combination of TiO₂ and metal catalyst with interfacial properties that match the combined hydrogenation and redox requirements for HDO of furfuryl alcohol. We vary the underlying metal surface across late transition metals and Pd overlayers to alter interfacial properties. The synergy between the oxide and metals’ functionalities towards the overall HDO catalytic cycle is demonstrated via electronic, physical and chemical descriptors - work function (Φ), oxygen vacancy formation energy (ΔE_{vac}), metal-carbon binding energy (M-C_{B.E.}), and the extent of metal-metal oxide interfacial charge transfer (q). HDO reaction energetics are linearly regressed against these descriptors. An optimal TiO₂/metal bifunctional catalyst is predicted for experimentally relevant HDO reaction conditions through simplified kinetic analyses, illustrating the trade-off among the examined descriptors that optimizes the overall catalytic cycle.

2. Computational Methods:

2.1. Electronic Structure Methods:

Spin polarized plane-wave DFT calculations were carried out using the Vienna Ab Initio Simulation Package (VASP), version 5.4.4. The electron exchange and correlation energies were computed using the Perdew, Burke, and Ernzerhof (PBE) version of the generalized gradient approximation (GGA) functional¹⁷ with dispersion corrections, PBE-D3.¹⁸ The projector augmented-wave (PAW)¹⁹ method was used to represent the ion-core electron interactions. Structures were considered converged with atomic forces less than 0.05 eV \AA^{-1} for all unconstrained atoms. The DFT+U method²⁰ within VASP was used for Ti d states with a $U_{\text{eff}} = 2 \text{ eV}$ to correct for on-site coulombic interactions, as suggested by Hu and Metiu.²¹ Also, U_{eff} values of 4.3,²² 3.3²³ and 5.3 eV^{24} were used for the d states of Fe, Co and Ni atoms, respectively. For transition metals Ti, Fe and Ni, 3p, 3d and 4s electrons were treated as valence electrons while for other transition metals, only outer shell d and s electrons were treated as valence electrons. Oxygen 2s and 2p electrons were treated as valence electrons. A plane wave energy cutoff of 450 eV was used to represent the valence electrons and a Monkhorst-Pack²⁵ k-point mesh of $2 \times 3 \times 1$ was used with the third vector perpendicular to the surface for all models. The k-point grid was confirmed to be converged using the 5×4 Pd(111) surface cell for testing. The same PBE+D3+(U for Ti, Fe, Ni, and Co) approach was used for both examining HDO reaction chemistry and determination of descriptor values. Transition states were located using the climbing image nudged elastic band (CI-NEB) method²⁶ (5-7 images) and the dimer method²⁷ by relaxing the reaction tangent force below 0.05 eV \AA^{-1} . Transition states were verified to contain a single imaginary frequency along the reaction coordinate.

2.2. Surface Models

2.2.1. Bare Metal Surface Models

A four layered, 5x4 FCC(111) slab was used to calculate the carbon binding energy and work function for Ag, Au, Cu, Pd, Rh, Ru and Zn. The cell configuration was chosen to match that used for the interfacial nanorod-TiO₂/metal interface model. All metals were simulated at an optimized Pd FCC bulk lattice constant of 3.952 Å. The metal lattice constant was kept at the Pd value to facilitate construction of a consistent interfacial model with TiO₂ (**Figure 2**), avoiding variation of the interfacial lattice strain due to the differences in lattice parameters between the metals and the TiO₂ nanorod. 20 Å of vacuum space was included in the direction perpendicular to the surface (**Figure S1a**). The atomic positions on the bottom two layers were frozen at their bulk lattice positions during structural optimizations.

Closed pack monolayer surfaces of Ag, Au, Co, Cu, Fe, Ir, Ni, Pt, Rh, Ru and Zn metals were also modeled atop a Pd (111) surface to form another bare surface model, hereafter termed as an M_{ML}-Pd (111) model. The optimized Pd FCC bulk lattice constant of 3.952 Å was used for the underlying Pd. Consistent with the M (111) model, this model used a four layered 5 × 4 FCC slab, separated by 20 Å of vacuum space in the direction normal to the surface (**Figure S1b**). The atomic positions on the bottom two layers were frozen at their bulk lattice positions. Carbon binding energies and work functions were also calculated over this surface model.

2.2.2. Rutile-TiO₂ Nanorod over Metal (111) and M_{ML}-Pd (111) Surface (TiO₂/M Model and TiO₂/M_{ML}-Pd Model)

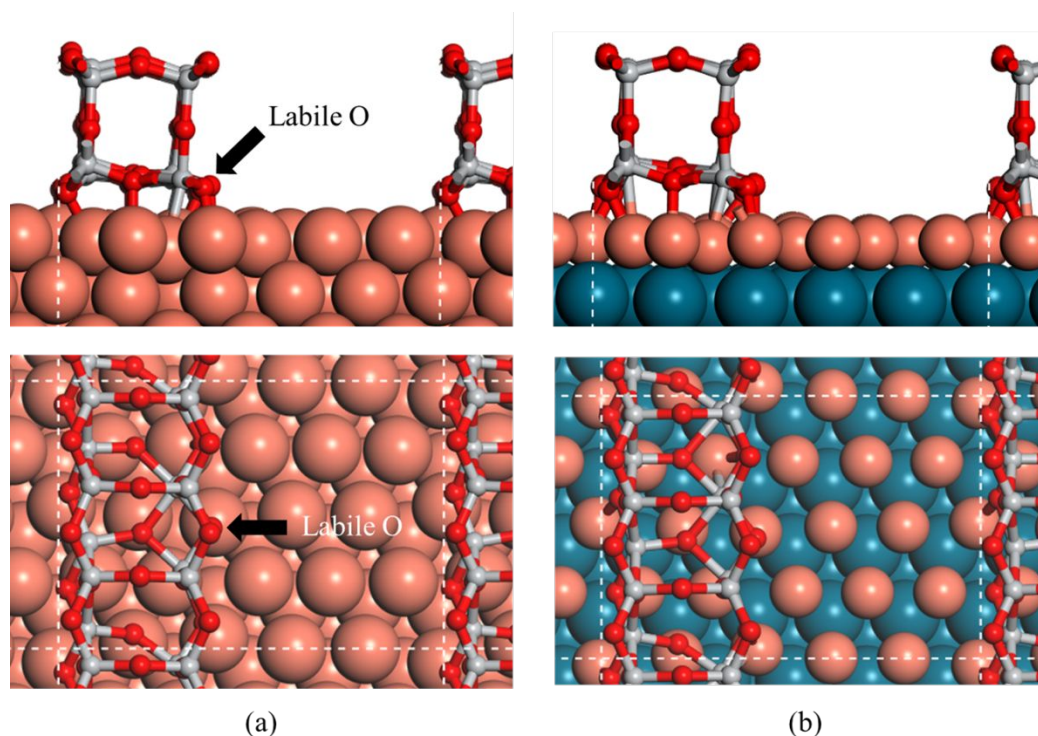


Figure 2. The DFT model for a rutile-TiO₂ nanorod over a) closed pack metals surfaces (TiO₂/M (111) model) and b) closed pack monolayers atop Pd (111) (TiO₂/M_{ML}-Pd (111) model). Color code: orange represents a generalized metal, blue represents Pd, gray represents Ti, and red represents O.

The interfacial sites between the different metals and TiO₂ are represented through an inverse DFT model in which a TiO₂ nanorod is placed over the closed pack metal surfaces of Ag, Au, Cu, Pd, Rh, Ru and Zn from the M (111) model. The strategy for building this interfacial model has been examined most extensively in our recent work on the deoxygenation of furfuryl alcohol modeled at a TiO₂/Pd interface,¹² and mimics a similar approach used previously for a SnO_x/Pt model by Vandichel et al.²⁸ to study low temperature CO oxidation. This prior work examined the nanorod/metal lattice match, and compared the TiO₂ nanorod/Pd(111) model to alternative models of the titania/metal interface (Pd nanorod adsorbed to TiO₂, small clusters of TiO₂ adsorbed on

Pd(111), and inert He pore models on Pd(111)). This work reached the conclusion that this model captured well the interfacial HDO chemistry, albeit still representing a model system of what is surely a complex, heterogeneous structure in Pd core-TiO₂ shell or Pd nanoparticle/TiO₂ support catalytic systems.

The adsorbed nanorod has two TiO₂ layers in each non-periodic direction, and each face exposes a (110) surface, both to the vacuum/adsorbates and to the metal surface (**Figure 2a**). The atomic positions of the bottom two metal layers were frozen at their bulk lattice positions, with the topmost two metal layers, the TiO₂ nanorod, and any adsorbates relaxed during structural optimizations. An equivalent model, shown in **Figure 2b**, was constructed for the TiO₂/M_{ML}-Pd (111) interface from the closed pack monolayers of Ag, Au, Co, Cu, Fe, Ir, Ni, Pt, Rh, Ru and Zn metals over the Pd (111) model. The overlayer model allows us to expand the data set examining HDO energetics beyond the set of pure metals, and, with the lattice constant set by the underlying Pd, avoids variations in lattice mismatch between the metal and the TiO₂ nanorod. As will be shown later in Section 3, the two interfacial models performed similarly for HDO chemistry, suggesting that constraining the pure metal surfaces to the Pd lattice constant does not dictate the observed trends.

The oxygen atom designated as *labile O* in **Figure 2a** is part of the TiO₂ nanorod and is bound to the metal surface. 6 symmetry equivalent interfacial oxygen atoms are present, though they differ slightly in their local coordination due to the lattice mismatch between the nanorod and underlying (111) surface. Our previous study found removal of this labile O atom to lead to the lowest vacancy formation energy, with an oxygen vacancy formation energy rather similar to that for an O atom on the surface of an extended rutile-TiO₂(110) surface near to an adsorbed Pd nanorod.¹² We consider O vacancy formation at this site and use this vacant site as an O-acceptor during breaking of the C-O bond during HDO.

2.3. HDO Reaction Schematic and Energetics

We first review the key steps involved in catalytic HDO before detailing our approach for calculating their energetics. The key steps of interfacial HDO include i) C-OH scission at an interfacial O vacancy (referred to as DDO, direct deoxygenation), ii) C-H formation (to form 2-methylfuran) and iii) H₂ activation/O vacancy generation to recreate the reduced O-vacant interfacial site. The key HDO steps and the associated reactants, intermediates and products are shown in **Figure 3**. The mechanism of HDO and energetics of these elementary steps have been studied in detail, with comparison to energetics on the Pd(111) surface, in our previous work using this TiO₂/Pd interfacial model.¹² DFT calculations of stable intermediates and transition states are used to evaluate the energetics for these three key steps across the range of TiO₂/metal interfaces. These reaction energies and activation barriers are defined, relative to gas phase furfuryl alcohol and hydrogen reactants, using equations 5, 6 and 7 and 8.

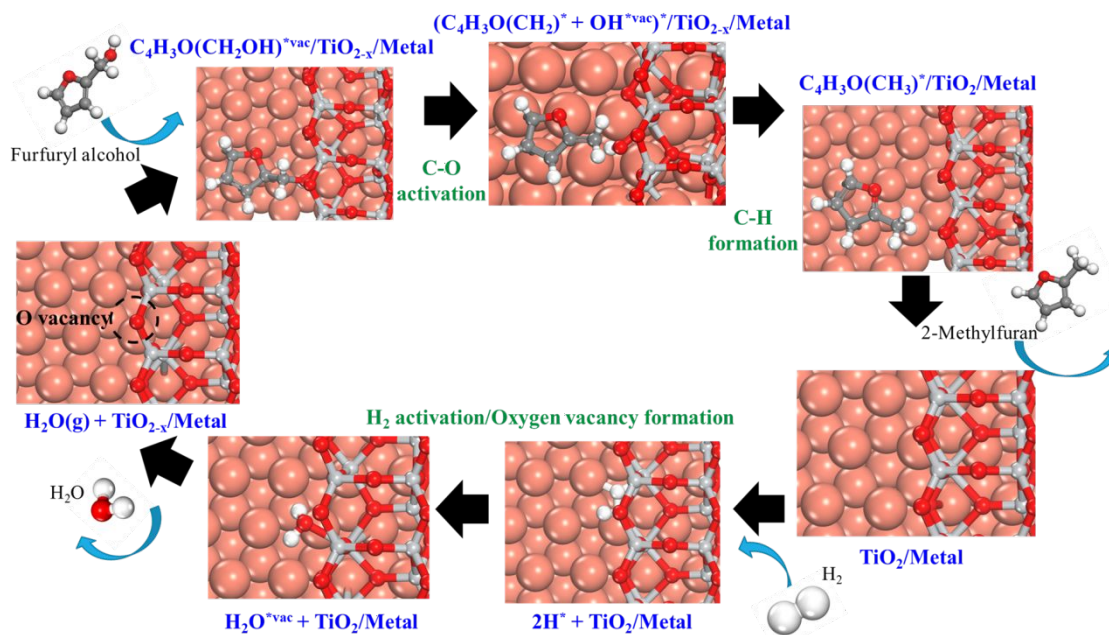


Figure 3. HDO catalytic cycle showing the major elementary steps - C-O activation, C-H formation and H₂ activation/oxygen vacancy formation over a TiO₂/metal interface model. Here, the interface model is meant to represent both interfacial DFT models - TiO₂/M and TiO₂/M_{ML}-Pd models. The associated reactants (furfuryl alcohol, C₄H₃O(CH₂OH) and H₂), intermediates and products (H₂O and 2-methylfuran, C₄H₃O(CH₃)) are shown for each of the steps.

Equation 5 defines the stability of the DDO transition state ($\Delta E_{TS, DDO}$):

$$\Delta E_{TS, DDO} = E_{TS} - E_{Furfuryl\ alcohol} - E_{Ovac, surface} \quad 5$$

where E_{TS} , $E_{furfuryl\ alcohol}$ and $E_{Ovac, surface}$ refer to the DFT energies of the DDO transition state structure, the gas phase furfuryl alcohol and the bare O deficient interface surface (TiO_{2-x}/M or TiO_{2-x}/M_{ML}-Pd), respectively. Equation 6 defines the relative stability of the C-H bond formation transition state ($\Delta E_{TS, C-H}$):

11

$$\Delta E_{TS, C-H} = E_{TS} - E_{Furfuryl\ alcohol} - E_{surface} + E_{H_2O} - E_{H_2} \quad 6$$

where E_{TS} , $E_{furfuryl\ alcohol}$, $E_{surface}$, E_{H_2O} and E_{H_2} refer to the DFT energies of the transition state structure for C-H formation, the gas phase furfuryl alcohol, the bare stoichiometric interface surface (TiO₂/M and TiO₂/M_{ML}-Pd), and the gas phase water and hydrogen gas, respectively. Our emphasis in searching for descriptors of transition state stability is to predict how the stability of the transition state differs among catalyst formulations and structures, such that the specific gas phase reference used would cancel in comparing among catalysts. The choice of gas phase reference alters the intercepts of such correlations (see Section 3.3 for use of equation 6), which are not emphasized in our search for descriptors.

The H₂ dissociation energetics ($\Delta E_{2H-diss}$) were reported in terms of a dissociative adsorption energy of H₂ over a stoichiometric interface as follows.

$$\Delta E_{2H-diss} = E_{H_2+surface} - E_{H_2} - E_{surface} \quad 7$$

where $E_{H_2+surface}$, E_{H_2} and $E_{surface}$ refer to the DFT energies of the H₂ adsorbed structure, the gas phase hydrogen, and the bare stoichiometric interface surface (TiO₂/M and TiO₂/M_{ML}-Pd) respectively. The gas phase energies of all molecular species were calculated by isolating the molecule in a large unit cell. The oxygen vacancy formation energy (ΔE_{vac}) was calculated for the “labile” O in **Figure 2**, as the energy to desorb an oxygen atom as 1/2 of an oxygen molecule:



Though equations 5-7 define the stability of the key transition states (DDO or C-H formation) or intermediate states (interfacial O vacancy) relative to gas phase reactants, the discussion of results will also involve reference to adsorption energies and elementary step reaction energies and activation barriers. Adsorption energies are calculated using their typical definition:

12

$$E_{ads,molecule} = E_{molecule + surface} - E_{molecule} - E_{surface} \quad 9$$

Reaction energies and activation barriers are calculated as:

$$\Delta E_{rxn} = \Delta E_{final} - \Delta E_{initial} \quad 10$$

$$\Delta E_{act} = \Delta E_{TS} - \Delta E_{initial} \quad 11$$

All energetics reported here are without ZPVE (Zero-point vibration energy) corrections unless mentioned otherwise. Since our discussion emphasizes trends across metals rather than the absolute values, it is a reasonable assumption that these corrections would be relatively constant across metals and therefore, not alter the trends.

2.4. Catalytic descriptors

We considered four “descriptors” for their potential to predict the HDO energetics. The metal work function (Φ) and metal-carbon binding energy ($M-C_{B.E.}$) were computed using the metal surface models without the nanorod included. The TiO_2/M and $TiO_2/M_{ML}-Pd$ interfacial models were used to calculate the interfacial oxygen vacancy formation energy (ΔE_{vac}) and extent of interfacial charge transfer (q).

The work function (Φ) is defined as the minimum energy required to move an electron from the surface to vacuum, and was calculated by correcting the Fermi level of the bare periodic slabs to a reference plane at the center of the vacuum region:

$$\Phi = |E_v - E_f| \quad 12$$

E_v is the energy in the vacuum, and E_f is the fermi energy. Work function was calculated for the bare close packed surfaces, M (111), and the metal monolayers atop Pd (111), $M_{ML}-Pd$ (111). The

C binding energy was calculated for C atom adsorption to an FCC hollow site over the M (111) and the M_{ML} -Pd (111) bare surface models, using Equation 8 with the DFT energy of a single carbon atom in vacuum as the reference. **Figure S2** shows the correlation between C binding energies on the bare metal surfaces and those including the interfacial site model. Though deviations are not insignificant (mean absolute deviation from parity is 0.41 eV), the deviation is relatively small in comparison to the span of C binding energies across the models (~5.5 eV). We have chosen to use the C binding energies on the bare slab as the descriptor as these would have more predictive power in allowing the use of tabulated M-C binding energies for other metal surfaces not included in our study. The extent of charge transfer between the TiO_2 nanorod and the metal surface was the fourth descriptor considered. As we showed in our prior work, oxygen vacancy formation caused excess charge accumulation in the Pd surface,¹² consistent with a perspective study by Puigdollers et al.²⁹ The excess metal charge (relative to the sum of valence electrons in neutral metal) (q) was quantified by summing the assigned Bader charges³⁰ over all the metallic atoms in the four layers of the unit cell. The sign convention for q used is that a positive value of q reflects loss of electrons while a negative q value represents a gain of electrons. The value of q was calculated for the O-vacant interfacial surface model.

3. Results and discussion:

We seek to examine correlations between the TiO_2 /metal interfacial descriptors and HDO energetics. In section 3.1, we report the values of the descriptors and analyze correlations among them to check their independence in representing interfacial properties. Sections 3.2, 3.3 and 3.4 then report the energetics associated with the three key HDO steps, C-O activation, C-H formation, and hydrogen activation/O vacancy formation, and examine their correlation with descriptors. In

section 3.5, we analyze the implications of the computed HDO/descriptor correlations under different kinetic regimes with a simplified kinetic analysis. Finally, Section 3.6 discusses design considerations relative to the reported descriptors and kinetic analysis in considering HDO catalyst formulation for optimal activity.

Throughout our study, we have considered a low coverage of hydrogen, with H^* co-adsorbed only when needed. Roughly estimated, the simulated coverage is 1 H per 16 metal atoms across the interfacial models. Furfuryl alcohol and its derived intermediates were also studied at low coverage. The implications of other reaction conditions over the HDO activity are discussed in Section 3.5. Structures of the key adsorbed intermediates (initial and final states) and transition states (TS) for the C-O activation, C-H formation and H_2 activation steps across the TiO_2/M (111) and the TiO_2/M_{ML} -Pd (111) interface models are illustrated in **Tables S5-7**, respectively.

3.1. Correlations among catalytic descriptors

Prior to examining HDO energetics, we analyze any correlations among the four considered descriptors to evaluate the extent to which they can be used to independently predict catalytic properties.

The values of the four descriptors considered for the TiO_2/M and TiO_2/M_{ML} -Pd catalysts are tabulated in **Table S1**. The work function values for the M (111) models are consistent with the experimentally reported values by Michaelson et. al.³¹ The metallic monolayers over Pd (111) gave a range of values for the work function, between 3.98 eV for the Ni monolayer and 5.9 eV for the Ir monolayer. Oxygen vacancy formation energies ranged between 2.04 eV – 4.35 eV, a considerable span about the value of the $TiO_2/Pd(111)$ surface (3.04 eV) that likely ranges across

systems with high and low interfacial O vacancy concentrations under HDO conditions. Across the oxygen-vacant interface models, the charge transfer to the metal surface ranged from a gain of electrons ($0.59 e^-$ for the Ir_{ML}/Pd) to a maximum loss of $2.50 e^-$ for the Fe_{ML}/Pd surface. The M-C_{B.E.} energies for the M (111) models are within 0.5 eV of the theoretically reported values in the literature, with consideration of similar adsorption sites over the closed pack metal surfaces.³² The metallic monolayers atop Pd (111) showed a wide range of C binding energies, from -3.5 eV for Ag to -8.52 eV for Ru.

Correlations between the four catalytic descriptors were examined by calculating 6 pairwise Pearson correlation coefficients, ρ (**Figure 4**). The coefficients determine the extent to which two descriptors are correlated. ρ with absolute value greater than 0.8 indicates a strong correlation and absolute values less than 0.5 suggest a weak correlation. A detailed statistical definition is provided in the SI. The correlation matrix in **Figure 4** shows that the descriptors Φ and q correlate very strongly in an inverse linear fashion ($\rho \sim -0.83$). This correlation might be expected, as a higher workfunction surface would be expected to better stabilize electrons transferred from the oxide following vacancy formation. We, therefore, do not consider these as independent descriptors in our analysis below, and use them somewhat interchangeably in discussing what dictates catalyst performance. The descriptors Φ and ΔE_{vac} also correlate very strongly in an inverse linear fashion ($\rho \sim -0.84$). Though both ΔE_{vac} and q correlate with Φ , the correlation between ΔE_{vac} and q themselves is weak ($\rho \sim 0.66$). M-C_{B.E.} does not correlate well with q or Φ . Their interdependence suggests that only one of ΔE_{vac} , Φ and q can be considered as an independent descriptor along with the metal-carbon binding energy (M-C_{B.E.}) as a second descriptor. Predominantly, we will use the descriptors Φ and M-C_{B.E.} to analyze their ability to predict HDO energetics, though we consider correlations with the other two descriptors as well (**Table S2**, **Table S3** and **Table S4**). While examining the dependence on more than 1 descriptor, all descriptors were standardized by removing the mean and scaling the values to unit variance. This was achieved by

16

scaling the sample 'x' to $(x - \text{mean})/\text{S.D.}$ where S.D. and mean correspond to the standard deviation and mean of all values within each category of descriptor, respectively. The interdependency between the catalytic descriptors is also shown in **Figure S3** where the descriptors are plotted against one another.

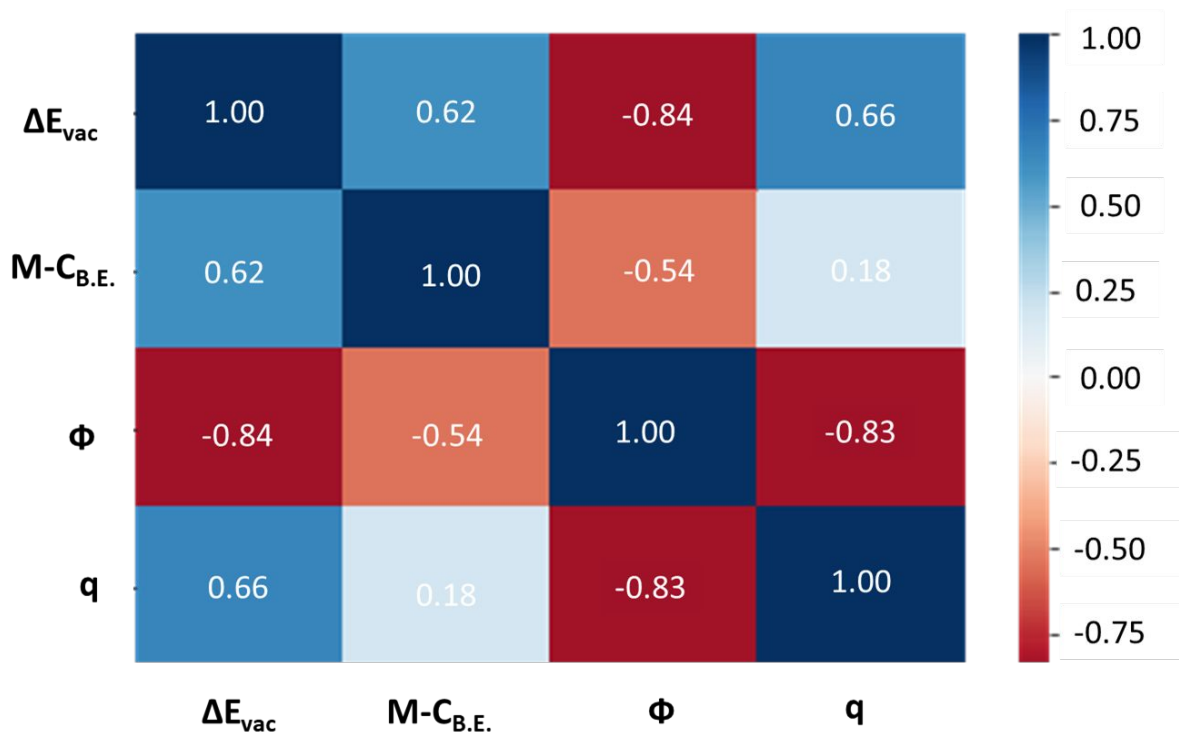


Figure 4. Pearson correlations coefficients between every pair of catalytic descriptors - work function (Φ), oxygen vacancy formation energy (ΔE_{vac}), metal-carbon binding energy (M-C_{B.E.}), and the extent of charge transfer (q).

3.2. DDO transition state stability correlates with metal workfunction.

The C-OH bond breaking step is significant in dictating both the activity and selectivity towards hydrodeoxygenation of furfuryl alcohol. **Figure 5a** shows a typical TS structure for C-

OH activation, in which the departing hydroxyl group partially fills the oxygen vacancy. The metallic surface binds the organic fragment, utilizing both the oxide and metal interfacial functionality to enable deoxygenation. **Figure 5c** shows a strong linear correlation between the underlying metal workfunction and the TS stability, with a larger workfunction predicting a more stable transition state ($\Delta E_{\text{TS-DDO}} = -0.94 \Phi + 2.78$, $R^2 = 0.85$). A higher metal work function (i.e., lower energy for incremental charge added to the metal) causes greater charge transfer into the metal surface, which in turn stabilizes the partial filling of the O vacancy during CO-activation. As the metal workfunction and the amount of charge transfer into the metal in the oxygen vacant surface strongly correlate, $\Delta E_{\text{TS-DDO}}$ also correlates very strongly with q (**Figure S4**), with a more negative q (higher negative charge transfer into metals) favoring TS stability. **Figure 5b** shows a charge density difference plot between the DDO transition state structure and separate single-point calculations of the interface and hydrocarbon moieties in the TS structure for the $\text{TiO}_2\text{-Rh}$ (111) interface. This difference plot shows significant charge transfer with the metal surface is involved in the interface stabilizing the transition state. The Bader charge density difference plots for TS structures across the TiO_2/M (111) model surfaces are shown in **Figure S5** and are qualitatively similar to **Figure 5b**. We note that the trend in DDO TS stability versus metal workfunction may be counterintuitive, given that a higher workfunction stabilizes vacancy formation (see **Section 3.1** and discussion in **Section 3.6**). A more stable oxygen vacancy might be expected to lead to a less stable DDO transition state, given that DDO re-oxidizes the vacancy. However, as noted above, the charge transfer to the metal that occurs during vacancy formation is not reversed at the DDO transition state, resulting in the somewhat counterintuitive trend in which factors that increase vacancy stability also stabilize the DDO transition state.

18

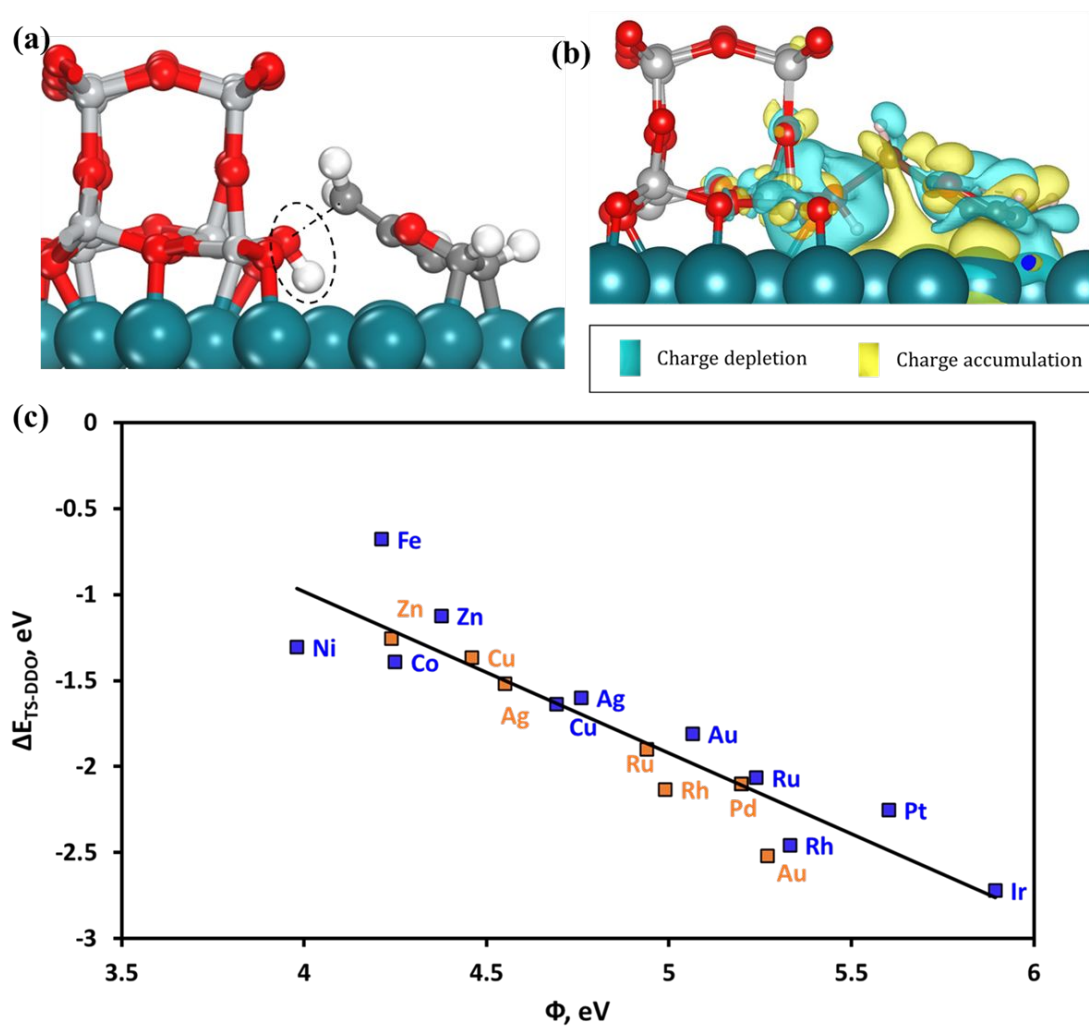


Figure 5. The transition state for DDO is examined at the TiO₂/metal interface. a) The C-OH activation TS state of furfuryl alcohol over the TiO₂-Rh (111) interface. The dotted oval represents the O vacancy which is filled in the process. b) A Bader charge density difference plot during the C-O activation TS over the TiO₂-Rh (111) interface. The isosurface level is 0.0013 e Bohr⁻³. The charge density difference plot is generated through the difference of charge between the DDO transition state structure and separate single-point calculations of the interface and hydrocarbon moieties in the TS structure. The light cyan and yellow colors indicate charge depletion and accumulation, respectively. c) gas phase stability of the C-OH DDO TS, $\Delta E_{\text{TS-DDO}}$, vs metal work function, Φ showing a linear correlation ($\Delta E_{\text{TS-DDO}} = -0.94 \Phi + 2.78$ and the $R^2 = 0.85$). Orange data points represent TiO₂/M(111) interface models and blue data points represent TiO₂/M_{ML}-Pd(111) models.

As the hydrocarbon fragment interacts with the metal surface at the transition state, we also considered using both the workfunction and metal-carbon binding energies as descriptors to predict the transition state stability. **Equation 13** ($R^2 = 0.85$ with a lower mean absolute error, MAE) shows a small improvement in predicting the transition state stability, with a small correlation coefficient for the added $M-C_{B.E.}$ descriptor:

$$\Delta E_{TS-DDO} = -1.79 + 0.01 M-C_{B.E.} - 0.47 \Phi \quad 13$$

Though equation 13 shows a possible small roll for $M-C_{B.E.}$ in dictating the DDO transition state stability, the metal work function is clearly the dominant descriptor. **Table S2** lists other linear fits for the DDO TS stability that include combinations of the 4 descriptors, including ΔE_{vac} and q . The fit is not improved relative to **equation 13** by including other descriptors. Structures of the key adsorbed intermediates (initial and final states) and transition states (TS) for the C-O activation step across the $TiO_2/M(111)$ and the $TiO_2/M_{ML}-Pd(111)$ interface models are illustrated in **Table S5**.

3.3. Metal-Carbon Binding Energy Describes Final C-H Formation

After the C-O bond of furfuryl alcohol is broken during deoxygenation, H^* bound near the interface is added to the methyl carbon of the adsorbed 2-methylfuryl species $C_4H_3O(CH_2)^*$ to form 2-methylfuran. A typical TS structure for this C-H bond formation is shown in **Figure 6**. At this transition state, the aromatic ring of the organic fragment is bound with the plane of the ring parallel to the surface. The methyl carbon is atop a metal atom, and the surface-C bond is extended as the new C-H bond is partially formed. The H^* species shares the same metal atom as the methyl C at

20

the transition state. As shown in **Figure 6**, a strong binding energy of C to the surface is a predictor of a more stable C-H formation transition state. A direct linear dependence of $\Delta E_{\text{TS-C-H}}$ with $M\text{-}C_{\text{B.E.}}$ is shown in **Figure 6** ($\Delta E_{\text{TS-C-H}} = 0.58 M\text{-}C_{\text{B.E.}} + 2.15$, $R^2 = 0.86$). As both the aromatic ring and the methyl C bind to the surface through C atoms, it is not surprising to see strong C binding as a predictor for a stable transition state.

The metal workfunction is a secondary descriptor for the C-H formation transition state stability. Adsorbed H^* leads to a small reduction of the metal surface, increasing the electron density on the metal such that a larger workfunction helps to stabilize the C-H formation transition state. This combined dependence on Φ and $M\text{-}C_{\text{B.E.}}$ is illustrated in the normalized correlation ($R^2 = 0.92$):

$$\Delta E_{\text{TS-C-H}} = -1.49 + 0.80 M\text{-}C_{\text{B.E.}} - 0.27 \Phi \quad 14$$

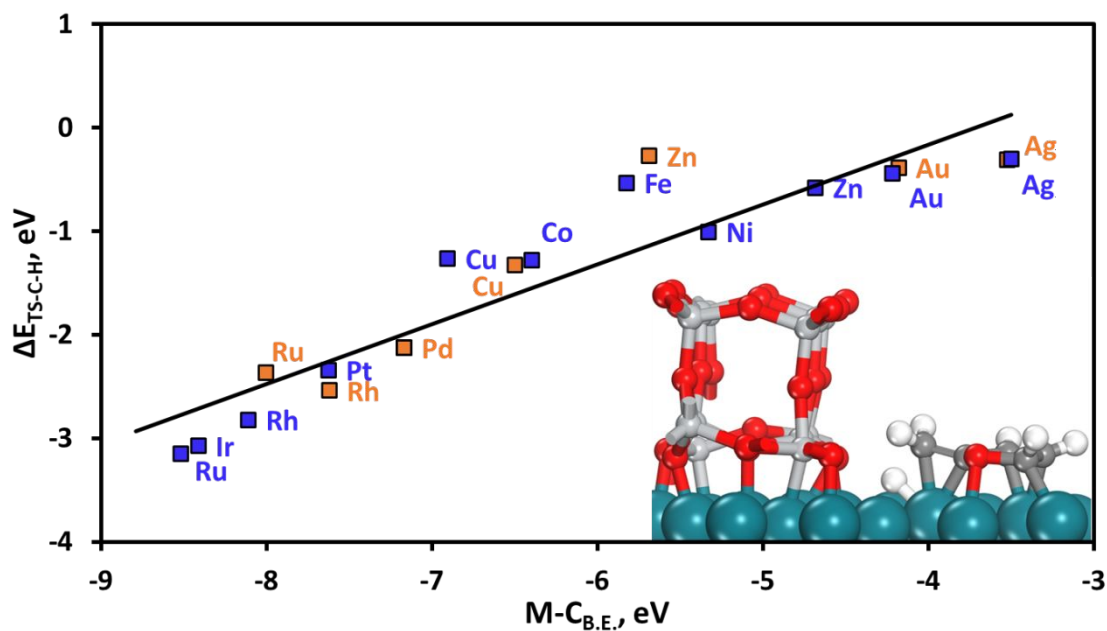


Figure 6. The stability of the C-H formation transition state, $\Delta E_{\text{TS-C-H}}$, is plotted versus the metal carbon binding strength, $M\text{-}C_{\text{B.E.}}$. The black line shows the linear correlation ($\Delta E_{\text{TS-C-H}} = 0.58 M\text{-}C_{\text{B.E.}} + 2.15$, $R^2 = 0.86$). Orange data points represent TiO_2/M (111) interface models and blue data points represent $\text{TiO}_2/\text{M}_{\text{ML}}\text{-Pd}$ (111) models. (inset) Example transition state structure for C-H formation to produce 2-methylfuran is shown for the TiO_2/Rh (111) model.

Table S3 lists other linear correlations that include $M\text{-}C_{\text{BE}}$, Φ , ΔE_{vac} and q as descriptors. As shown in the table, the fit is not improved significantly relative to **equation 14** by including the addition two descriptors. Structures of the key adsorbed intermediates (initial and final states) and transition states (TS) for the C-H formation step across the TiO_2/M (111) and the $\text{TiO}_2/\text{M}_{\text{ML}}\text{-Pd}$ (111) interface models are illustrated in **Table S6**.

3.4. Hydrogen Activation and Oxygen Vacancy Formation Energetics

After C-OH dissociation, the oxygen vacant active site is filled by the hydroxyl group of furfuryl alcohol, and the vacancy needs to be regenerated to enable the next HDO catalytic cycle. Oxygen vacancy formation will occur through H₂ adsorption and dissociation, followed by water formation and desorption. H₂ dissociates over the metal surface, and adsorbed H* can then “spill over” to TiO₂ and bind to an O²⁻ ion. **Figure 3** illustrates these intermediate structures - 2H* + TiO₂/Metal, H₂O*^{vac} + TiO₂/Metal and H₂O(g) + TiO_{2-x}/Metal). The overall reaction for O vacancy regeneration is TiO₂ + H₂ → TiO_{2-x} + H₂O.

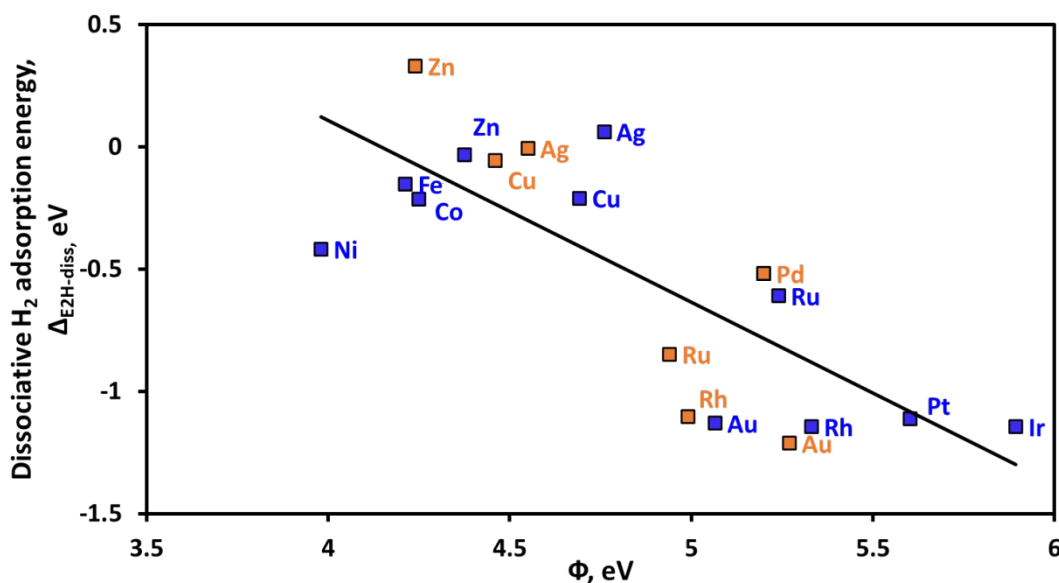


Figure 7. Dissociative hydrogen adsorption energy vs metal work function. The black line shows the linear correlation ($\Delta E_{2H-diss} = -0.74 \Phi + 3.08$, $R^2 = 0.60$). Orange data points represent TiO₂/M(111) interface models and blue data points represent TiO₂/M_{ML}-Pd(111) models.

Figure 7 plots the dissociative adsorption energy of H₂ versus the metal work function. We considered the adsorbed state with one H* bound to the metal and the second H* bound to the labile interfacial O atom, as it has been recently shown that heterolytic activation of H₂ at metal-TiO₂ interfaces can occur over small barriers surmountable near room temperature.³³ We did not

compute transition states for this process, as H₂ activation is not expected to kinetically limit the HDO process.¹² Dissociative hydrogen adsorption reduces the surface; we therefore hypothesized that the dissociative adsorption energy would be predicted by the metal work function. There is a rough linear correlation of $\Delta E_{2H-diss}$ with the metal work function ($\Delta E_{2H-diss} = -0.74 \Phi + 3.08$, $R^2 = 0.60$), where higher work function favors H₂ dissociation (**Figure 7**). **Table S4** lists other linear fits that include combinations with the ΔE_{vac} and q descriptors. M-C_{B.E.} descriptor was not considered as a descriptor as there are no C atoms involved in H₂ adsorption. The prediction of dissociative H₂ adsorption is not improved significantly by including descriptors other than Φ .

We previously used DFT calculations for the TiO₂/Pd(111) interface to show that spillover of H to TiO₂ is energetically facile, and we did not compute the subsequent barriers or reaction energies for formation of the state with water adsorbed in the vacancy. However, as discussed below in considering trade-offs in interfacial HDO catalyst design, the vacancy formation processes might be approximated as equilibrated, with the overall vacancy formation reaction energy (ΔE_{vac}) indicating the relative concentration of vacant sites across different interfacial compositions. As discussed in **Section 3.1**, we considered ΔE_{vac} as a potential descriptor of HDO energetics, but found it strongly correlates with the metal work function in an inverse fashion ($\rho \sim -0.90$). A higher work function favors the generation of an O vacancy by lowering the energy of the electrons dispersed from Ti-O bonding into the metal surface. The linear correlations of ΔE_{vac} with Φ and q are shown in **Figure 8** and **Figure S3e**, respectively. Structures of dissociative H₂ adsorption for H₂ activation across the TiO₂/M (111) and the TiO₂/M_{ML}-Pd (111) interface models are illustrated in **Table S7**.

Figures 7 and 8 collectively show that a higher metal work function will promote O vacancy formation, either through promoting dissociative adsorption of H₂ or the overall O-vacancy formation process. O-vacancy formation, DDO transition state stability, and C-H formation

transition state stability were identified as the key energetics dictating the overall HDO catalytic process. Considered the correlations shown in Sections 3.2, 3.3, and 3.4, the metal work function and carbon binding energy are determined to be reliable descriptors for these three key energetics. In the next section, we discuss how these descriptors will dictate optimal HDO catalyst design under different kinetic operating regimes.

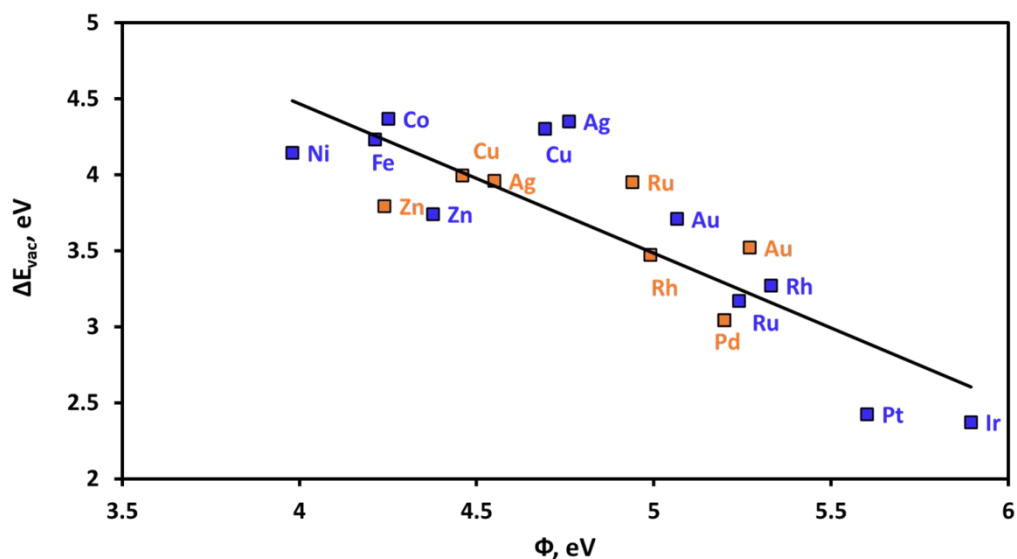


Figure 8. Oxygen vacancy formation energy of the interfacial model plotted against the metal work function, Φ . The black line shows the linear correlation ($\Delta E_{\text{vac}} = -0.98 \Phi + 8.40$, $R^2 = 0.72$). Orange data points represent $\text{TiO}_2/\text{M}(111)$ interface models and blue data points represent $\text{TiO}_2/\text{M}_{\text{ML}}\text{-Pd}(111)$ models.

3.5. HDO Kinetic Analysis and Descriptor Based Interfacial Catalyst Design

The previous sections examined descriptors predicting key energetics in the HDO catalytic cycle: the TS stabilities of deoxygenation (C-O dissociation) and methylfuran formation (C-H formation) and H₂ dissociation/oxygen vacancy formation. C-O dissociation and O-vacancy formation are both favored for surfaces with a higher workfunction, while a stronger metal-carbon

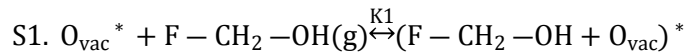
binding energy facilitates the C-H bond formation step. Metal workfunction and C-binding energy are effective descriptors for all of these key energetics. These descriptors are metal properties, as our models were constructed with the composition and structure of the TiO₂ nanorod, the oxide portion of the interface, constant across the models. **Table 1** illustrates the descriptors for these three key functionalities for an active HDO interfacial catalyst.

In this section, we perform a simplified kinetic analysis to examine how different catalytic regimes impact the trade-off in optimizing these descriptors for HDO performance. For simplicity, two different kinetic regimes are discussed – one with the C-O activation step being rate limiting and the other with the C-H formation being the rate determining step. We also consider how the governing rate expressions in each regime would be altered based on the reducibility of the interface. Under each scenario or reaction conditions, a dominant descriptor or a combination of descriptors that identifies the optimal HDO catalyst is reported where the kinetic regime operable in a specific HDO system would be dictated both by the interfacial HDO energetics and by the operating conditions (H₂, hydrocarbon, and water partial pressures and system temperature). An important assumption in our kinetic analysis is that the active site for HDO can be considered a collective interfacial site, rather than separately tracking the coverage of hydrocarbon and hydrogen adsorbates on the metal as well as H*, OH*, or oxygen vacancy species on the interfacial TiO₂. This is an approximation that proves useful in providing general guidance in interfacial site design, as discussed below.

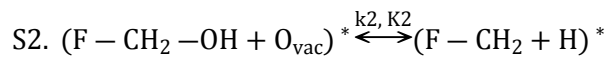
Reduced HDO reaction mechanism

To perform our kinetic analysis, we use a reduced reaction mechanism that incorporates the key HDO functionalities into lumped sequences of elementary steps. We begin the HDO catalytic

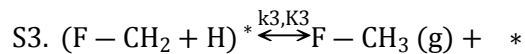
cycle with the elementary step S1, which is the adsorption of furfuryl alcohol near an interfacial O vacancy site.



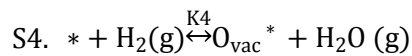
Step S2 is the elementary DDO step to break the C-O bond.



Step S3 includes the subsequent C-H formation and desorption of methyfurane, and lumping these steps makes the assumption that product desorption will not limit the HDO rate.



Next, to close the catalytic cycle and regenerate the oxygen vacancy, H₂ dissociative adsorption and oxygen vacancy formation can be considered as an equilibrated sequence of steps. Lumping these steps embeds the assumption that hydrogen adsorption, dissociation, H spillover (to form water precursor), and water desorption are collectively equilibrated, described within the overall oxygen vacancy formation reaction.



K_i denotes the equilibrium constant for the i th step and k_i denotes the forward rate constant for the i th step. “*” denotes an adsorbed state.

Table 1. A summary of the different interfacial HDO functionalities, their measure of energetics, relevant kinetic variables from steps S1-S4, descriptors (and normalized coefficients wherever combined dependence over two descriptors are shown) from the linear correlations defining those energetics from sections 3.2-3.4.

S. No.	Interfacial HDO functionality	Energetics measure	Relevant kinetic variables	Descriptor(s) (and normalized coefficients) from linear correlations	Section discussed
1	C-O bond activation	DDO TS stability, (ΔE_{TS-DDO})	$K1 \times k2$	Φ (-0.42), M-C _{B.E.} (0.02)	3.2 (Figure 5)
2	C-H formation	ΔE_{TS-C-H}	$K1 \times K2 \times k3 \times K4$	Φ (-0.23), M-C _{B.E.} (0.91)	3.3 (Figure 6)
3	Hydrogen activation and oxygen vacancy formation	$\Delta E_{2H-diss}$ and ΔE_{vac}	$K4$	Φ (-0.74, -0.98 respectively)	3.4 (Figures 7 and 8)

Rate expressions for the two different kinetic regimes

We consider kinetic regimes where either the DDO step (S2) or C-H formation step (S3) limit the overall HDO rate and use standard Langmuir-Hinshelwood catalytic kinetics to derive the operable rate expressions given the assumption of rate limiting step with mechanism S1-S4. With S2 the rate limiting step, the overall HDO rate can be expressed as:

$$\text{HDO rate} = \frac{(K1.k2) K3 K4 P_{H2} P_{FAL}}{K3 K4 P_{H2} + K1 K3 K4 P_{H2} P_{FAL} + P_{FCH3} P_{H2O} + K3 P_{H2O}} \quad 15$$

where P_j represents the partial pressure of species j in the reaction environment.

With C-H formation step (S3) as the rate limiting step, the overall HDO rate is given by:

28

$$\mathbf{HDO\ rate} = \frac{(K_1 K_2) k_3 K_4 P_{H_2} P_{FAL}}{K_4 P_{H_2} + K_1 K_4 P_{H_2} P_{FAL} + K_1 K_2 K_4 P_{H_2} P_{FAL} + P_{H_2O}} \quad 16$$

These rate expressions can be further reduced with assumptions as to the surface coverage under reaction conditions and the extent of surface reducibility. The mathematical manipulations that result in the reduction of the rate expressions under all considered scenarios are shown in Section S10. We consider three such scenarios.

Scenario 1: Interfacial site is highly reducible, and adsorbed hydrocarbon coverage is low.

For a scenario in which the interfacial site is highly reducible, and the adsorbed hydrocarbon coverage is low, if S2 is the rate determining step (RDS), then equation 15 reduces to

$$\mathbf{HDO\ rate} = (K_1 k_2) P_{FAL} \quad \textit{Scenario 1a, 17}$$

Here, the HDO rate is dictated by the TS stability of C-O activation (S2), relative to the oxygen vacant TiO_{2-x} /Metal surface and gas phase reactants. The DDO transition state stability computed in Section 3.2 represents the apparent activation barrier observed in this scenario. As discussed in Section 3.2, the metal work function dictates the relative performance of HDO catalysts in this scenario and improving HDO activity under this scenario would be achieved by using a metal with a higher work function.

If S3 is the rate determining step (RDS), then equation 16 reduces to

$$\mathbf{HDO\ rate} = (K_1 K_2) k_3 P_{FAL} \quad \textit{Scenario 1b, 18}$$

Multiplying and dividing the rate expression by K_4 converts the rate expression into $\frac{(K_1 K_2) k_3 K_4 P_{FAL}}{K_4}$,

where the numerator $(K_1 \times K_2) \times k_3 \times K_4$ combines to denote the gas phase-referenced TS stability of the C-H formation step, S3, which is dictated by the metal-carbon binding energy, $M-C_{B.E.}$

(**Figure 6**, Section 3.3). Although K_4 (for H_2 activation and oxygen vacancy formation) in the denominator points towards a lower metal workfunction for higher HDO activity, this results from the (arbitrary) sequence we used that places the final water desorption/oxygen vacancy formation step after the C-H formation step. These steps occur in parallel and are rather independence energetically. We verified that correlations for C-H transition state stability with C binding energy hold regardless of whether the O vacancy is present at the interface (**Figure S6**). If C-H formation was taken to occur after vacancy formation, K_4 would not appear in the denominator and the HDO rate would directly correlate with C-H formation energetics. Therefore, strong metal-carbon binding would drive the overall HDO activity under this reaction regime.

Scenario 2: Interfacial surface is not highly reducible, and adsorbed hydrocarbon coverage is low.

If S2 is the RDS, then equation 15 reduces to

$$\text{HDO rate} = \frac{(K_1 k_2) K_4 P_{H_2} P_{FAL}}{P_{H_2O}} \quad \text{Scenario 2a, 19}$$

In this scenario, both a more reducible surface (high K_4) and more stable DDO TS ($K_1 \times k_2$) would increase the rate of HDO. Both vacancy formation and DDO transition state stability are favored for a metal with a higher work function.

If S3 is the RDS, then equation 16 reduces to

$$\text{HDO rate} = \frac{(K_1 K_2 k_3) K_4 P_{H_2} P_{FAL}}{P_{H_2O}} \quad \text{Scenario 2b, 20}$$

Here, $(K_1 \times K_2) \times k_3 \times K_4$ combinedly denotes the gas phase TS stability of the C-H formation step, S3 which is dictated by strong metal-carbon binding, M-C_{B.E.} (**Figure 6**, Section 3.3). The

30

dependence on K_4 (reducibility) of the interface is lost here since during C-H formation (S3), an O vacancy generated in the elementary step S4 is re-filled by furfuryl alcohol's hydroxyl group through the elementary steps S1 and S2. Therefore, a strong metal-carbon binding alone would drive the overall HDO activity under this reaction regime.

Scenario 3: Hydrocarbon coverage is high.

When the hydrocarbon coverage on the surface is high, the terms that include P_{FAL} in equations 15 and 16 will dominate the denominator. If S2 is the RDS, then equation 15 reduces to

$$\text{HDO rate} = k_2 \quad \text{Scenario 3a, 21}$$

Here, HDO rate is dictated by k_2 , the activation barrier for C-O activation (S2). This activation barrier would be calculated as the energy difference between the DDO TS state ($\text{F} - \text{CH}_2 - \text{OH} + \text{O}_{\text{vac}}^\ddagger$) and the adsorbed state ($\text{F} - \text{CH}_2 - \text{OH} + \text{O}_{\text{vac}}^*$), which is not equivalent to the way the DDO TS stability was calculated in Section 3.2. The energies of both the DDO transition and the initial states correlate with the work function of the metal surface (Section 3.2, Figure 5c and Figure S7 respectively). The difference between the two correlations (Figure S8) introduces sufficient noise such that the calculated activation barriers show no significant correlation with the metal work function, with only a poorly fit and slight trend noted in a linear fit. If this roughly fit correlation is trusted more than the actual DFT data, or if an approximate guideline is desired, the metal work function serves as only a weak predictor of relative HDO activity under this kinetic scenario, where higher metal workfunction would slightly increase the value of k_2 .

If S3 is the RDS, then equation 16 reduces to

$$\text{HDO rate} = \frac{K_2 k_3}{(1 + K_2)} \quad \text{Scenario 3b, 22}$$

If C-O bond activation energetics are also favorable ($K_2 \gg 1$), the HDO rate expression reduces to k_3 which includes the activation barrier for the C-H formation (S3), defined as the energy difference between the TS state ($\text{F} - \text{CH}_2 + \text{H}$)[#] and the adsorbed state ($\text{F} - \text{CH}_2 + \text{H}$)^{*}. This is, however, not the C-H formation TS stability discussed in Section 3.3, as that value was referenced to gas phase species rather than the reaction initial state. Similar to the reasons mentioned under the scenario 3a, k_3 would correlate with M-C binding energy and the correlation can be used as a general guideline within the errors introduced while correlating with ΔE_{act} for step S3. Stronger metal-carbon binding energy alone (**Figure 6, Section 3.3**) would favor HDO activity if the C-H formation step is the rate determining step.

However, if C-O bond activation energetics are unfavorable ($K_2 \ll 1$, but C-H bond formation remains the RDS, kinetic analysis is complex. In this situation, the DDO step would be endothermic, but the TS for DDO not as high on a consistent relative energy scale as the transition state for C-H formation. The HDO rate expression would then reduce to $K_2 \times k_3$, and the dependence on the individual descriptors from sections 3.2 - 3.4 is not very straightforward. In addition to being dependent on k_3 as above, the HDO rate would also be dictated by K_2 , the reaction energy for the C-O activation step. This reaction energy is dictated by a combination of the descriptors Φ and $\text{M-C}_{\text{B.E.}}$ where higher Φ enables furfuryl alcohol adsorption near an O vacancy (**Figure S7**) and a stronger $\text{M-C}_{\text{B.E.}}$ drives the reaction energy by binding the methylic carbon of the methylfuryl fragment obtained after C-O bond breaking (**Figure S9**). Therefore, combining a higher Φ and a stronger $\text{M-C}_{\text{B.E.}}$ would dictate the HDO activity under this scenario.

Considering scenarios 1a, 2a, and 3a collectively, higher metal work function would contribute to promote HDO activity if the rate is limited by the DDO step. Under low hydrocarbon

coverage (Scenarios 1a and 2a), the work function is a sufficient and strong predictor of HDO activity when DDO is the rate limiting step. However, Scenario 3 illustrates that removing the approximation of low hydrocarbon coverage weakens the strength of work function as a descriptor, and the predictive ability of work function would attenuate as coverage increases. As adsorption of the large aromatic species is quite favorable on the active, high work function metals (Pt, Ir, Rh), a low coverage assumption would only be valid at rather low furfuryl alcohol pressures or high temperatures.

When scenarios 1b, 2b, and 3b are considered collectively, stronger metal-carbon binding energy contributes to promote HDO activity in the limit of the C-H formation step being the RDS. Under low hydrocarbon coverage (Scenarios 1b and 2b), the $M-C_{B.E.}$ is a sufficient and strong predictor of HDO activity when C-H formation is rate limiting. However, Scenario 3 with high hydrocarbon coverage shows a dependence on whether the preceding step of C-O activation is favorable. Accordingly, $M-C_{B.E.}$ controls the kinetics together with the metal workfunction when it is less favorable to deoxygenate as well.

The various HDO reaction scenarios, and the respective descriptors and HDO rate expressions dictating the rates under those scenarios through our simplified rate analysis are summarized in **Table 2**.

Table 2. A summary of the different HDO reaction scenarios, the simplified rate analysis and the descriptors dictating the rates under each scenario and HDO rate expressions (with equations numbered from **Section 3.5**) under relevant rate determining steps.

S. No. (Equations)	Reaction condition 1	Reaction conditions 2	Rate determining step	Descriptor(s)	HDO rate expression
1a-b, 17-18	Low hydrocarbon coverage	Interfacial surface is highly reducible (<i>scenario 1</i>)	C-O bond activation (S2)	Φ	$(K1 k2) P_{FAL}$
			C-H formation (S3)	$M-C_{B.E.}$	$(K1 K2) k3 P_{FAL}$
2a-b, 19-20	Low hydrocarbon coverage	Interfacial surface is not highly reducible (<i>scenario 2</i>)	C-O bond activation (S2)	Φ	$\frac{(K1 k2) K4 P_{H2} P_{FAL}}{P_{H2O}}$
			C-H formation (S3)	$M-C_{B.E.}$	$\frac{(K1 K2 k3) K4 P_{H2} P_{FAL}}{P_{H2O}}$
3a-b, 21-22	High hydrocarbon coverage	Interfacial surface is either highly reducible or not (<i>scenario 3</i>)	C-O bond activation (S2)	Φ	$k2$
			C-H formation (S3)	$M-C_{B.E.}^*, \Phi^{**}$ & $M-C_{B.E.}^{**}$	$k3^*$ or $K2 k3^{**}$

* $k3$ depends on $M-C_{B.E.}$ ($K2 \gg 1$, favorable C-O activation) as discussed under the relevant section for the discussion of scenario 3b.

** For $K2 \ll 1$, the dependence over the descriptors is not straightforward. Please refer to the relevant section where scenario 3b is discussed.

3.6. Optimal TiO₂/metal Interface for Hydrodeoxygenation

In the previous section, we discussed the different reaction conditions and reaction regimes where our descriptor-based analysis from Sections 3.2 - 3.4 is useful to predict the HDO performance of an interfacial catalyst. A single dominant descriptor or a combination of descriptors out of ΔE_{vac} , Φ , q and $M-C_{B.E.}$ would determine the overall HDO activity under the above scenarios. The linear correlations from **Figures 5c** and **6** indicate that a higher Φ metal and stronger $M-C_{B.E.}$ respectively would provide an optimal TiO₂/metal catalytic interface. Since the descriptors Φ and

$M-C_{B,E}$ do not correlate (Section 3.1), they are independent rather than competing in choosing the optimal material for HDO catalysis.

For reaction conditions leading to a low hydrocarbon coverage (scenario 1), such as a high H_2 /hydrocarbon stoichiometric ratio, an optimal HDO catalyst is dictated through higher metal Φ and stronger $M-C_{B,E}$. Rh, Ru, Pd and Pt interfaced with TiO_2 meet both criteria. These metals have long been studied for HDO reactions and are particularly active. Because of higher Φ , these interfacial systems are also highly reducible with lower ΔE_{vac} as shown in **Figure 8**. Au has a higher work function; however, it binds carbon atoms very weakly (**Figure 6**). Bimetallic core-shell systems³⁴ with a Rh, Ru or Pt monolayer atop Pd are proposed to offer tunable properties towards even higher Φ and stronger $M-C_{B,E}$ than monometallic Pd and are, therefore, predicted to be more active towards HDO than the monometallic components.

If the adsorbed hydrocarbon coverage is high, the activation barriers for C-O bond breaking or C-H formation (**Figure S8** and **Figure S10**, respectively) dictate the rate. Smaller differences among compositions then lead to weaker and less accurate dependence on the tested descriptors, though a higher metal Φ and stronger $M-C_{B,E}$ (e.g., Rh, Ru, Pt etc.) remain as weak descriptors of an effective catalyst, leading us to the same candidate catalysts.

A full microkinetic analysis would be needed to clarify the optimal catalyst when a single step is not rate-determining. Reaction regimes where HDO is limited by product desorption have not been considered. The HDO activity would then follow a volcano relationship with the metal carbon binding energy, trading off C-H bond formation activity for the ease of product desorption.

Learnings from our current interfacial model of TiO_2 with different metal surfaces could also be easily applied to other interfacial systems with a different reducible oxide. Scenario 2 in **Section 3.5** aims to successfully predict HDO activity for the cases where the oxide is not highly

reducible. There, the reducibility of the interface is recommended to be an important descriptor. Our work showed that reducibility, ΔE_{vac} also depends on the metal work function, with higher metal Φ lowering the energetic cost to create interfacial vacancies (**Figure 8**). For also varying the oxide, a combination of intrinsic oxide reducibility and metal workfunction would be needed to predict the stability of interfacial vacancies. We speculate that similar predictive correlations shown herein would hold for different oxides, with varying slopes and intercepts based on the oxide's inherent reducibility.

4. Conclusions

Using our previously reported model of an oxide-metal interface catalyst – a TiO_2 nanorod on a Pd (111) surface,¹² we identified the material descriptors that dictate furfuryl alcohol HDO activity. By varying the metal component of the interface, we determined that the metal workfunction is a strong descriptor of interfacial C-O dissociation activity, whereas M-C binding energy is a descriptor for C-H bond formation activity. A high metal work function favors deoxygenation (C-O bond breaking step), and strong metal carbon binding favors the subsequent C-H formation. Higher metal work function also favors dissociative H_2 adsorption and oxygen vacancy formation. Among monometallic catalysts, this analysis suggests the well-known HDO activity for Pd, Pt, Rh and Ru catalysts. Monolayers of Pt, Rh, and Ru atop Pd are predicted to be more active than monometallic Pd catalysts. Such core-shell catalysts with oxide layered coatings provide avenue for further tuning the structural, electronic, and chemical properties of the interface (Φ and $\text{M-C}_{\text{B.E}}$ in our case).

5. Acknowledgements

The authors acknowledge support from the National Science Foundation for funding this research through DMREF Grant #1436206. We are also thankful to Prof. Will Medlin (University of Colorado Boulder), and Prof. Eranda Nikolla (Wayne State University) for feedback and useful discussions. This work used the Extreme Science and Engineering Discovery Environment (XSEDE), which is supported by National Science Foundation grant number ACI-1053575. S. Deo acknowledges training provided by the Computational Materials Education and Training (CoMET) NSF Research Traineeship (grant number DGE-1449785).

6. Conflicts of Interest

The authors declare no conflicts of interest.

7. References

1. J. Zhang, B. Wang, E. Nikolla and J. W. Medlin, *Angewandte Chemie*, 2017, **129**, 6694-6698.
2. M. J. Rasmussen and J. W. Medlin, *Catalysis Science & Technology*, 2020, **10**, 414-423.
3. C. Wang, A. V. Mironenko, A. Raizada, T. Chen, X. Mao, A. Padmanabhan, D. G. Vlachos, R. J. Gorte and J. M. Vohs, *ACS Catal.*, 2018, DOI: 10.1021/acscatal.8b01746, 7749-7759.
4. J. Fu, J. Lym, W. Zheng, K. Alexopoulos, A. V. Mironenko, N. Li, J. A. Boscoboinik, D. Su, R. T. Weber and D. G. Vlachos, *Nature Catalysis*, 2020, DOI: 10.1038/s41929-020-0445-x.
5. S. M. Schimming, O. D. LaMont, M. Konig, A. K. Rogers, A. D. D'Amico, M. M. Yung and C. Sievers, *ChemSusChem*, 2015, **8**, 2073-2083.
6. M. Lu, H. Du, B. Wei, J. Zhu, M. Li, Y. Shan, J. Shen and C. Song, *Industrial & Engineering Chemistry Research*, 2017, **56**, 12070-12079.
7. R. C. Nelson, B. Baek, P. Ruiz, B. Goundie, A. Brooks, M. C. Wheeler, B. G. Frederick, L. C. Grabow and R. N. Austin, *ACS Catal.*, 2015, **5**, 6509-6523.
8. A. J. R. Hensley, Y. Hong, R. Zhang, H. Zhang, J. Sun, Y. Wang and J.-S. McEwen, *ACS Catal.*, 2014, **4**, 3381-3392.
9. O. T. O., B. Byeongjin, G. L. C. and C. S. P., *ChemCatChem*, 2017, **9**, 2642-2651.
10. L. Giordano and G. Pacchioni, *Acc Chem Res*, 2011, **44**, 1244-1252.
11. D. Ricci, A. Bongiorno, G. Pacchioni and U. Landman, *Phys Rev Lett*, 2006, **97**, 036106.
12. S. Deo, W. Medlin, E. Nikolla and M. J. Janik, *Journal of Catalysis*, 2019, **377**, 28-40.
13. N. M. Briggs, L. Barrett, E. C. Wegener, L. V. Herrera, L. A. Gomez, J. T. Miller and S. P. Crossley, *Nat. Commun.*, 2018, **9**, 3827.
14. M. Lu, H. Du, B. Wei, J. Zhu, M. Li, Y. Shan and C. Song, *Energy & Fuels*, 2017, **31**, 10858-10865.
15. G. Kumar, E. Nikolla, S. Linic, J. W. Medlin and M. J. Janik, *ACS Catal.*, 2018, **8**, 3202-3208.
16. Y. Hong, H. Zhang, J. Sun, K. M. Ayman, A. J. R. Hensley, M. Gu, M. H. Engelhard, J.-S. McEwen and Y. Wang, *ACS Catal.*, 2014, **4**, 3335-3345.
17. J. P. Perdew and Y. Wang, *Physical Review B*, 1992, **45**, 13244-13249.
18. S. Grimme, J. Antony, S. Ehrlich and H. Krieg, *The Journal of Chemical Physics*, 2010, **132**, 154104.
19. P. E. Blöchl, *Physical Review B*, 1994, **50**, 17953-17979.
20. S. L. Dudarev, G. A. Botton, S. Y. Savrasov, C. J. Humphreys and A. P. Sutton, *Physical Review B*, 1998, **57**, 1505-1509.
21. Z. Hu and H. Metiu, *The Journal of Physical Chemistry C*, 2011, **115**, 5841-5845.
22. M. Cococcioni, A. Dal Corso and S. de Gironcoli, *Physical Review B*, 2003, **67**.
23. L. Wang, T. Maxisch and G. Ceder, *Physical Review B*, 2006, **73**.

24. O. Bengone, M. Alouani, P. Blöchl and J. Hugel, *Physical Review B*, 2000, **62**, 16392-16401.
25. H. J. Monkhorst and J. D. Pack, *Physical Review B*, 1976, **13**, 5188-5192.
26. G. Henkelman, B. P. Uberuaga and H. Jonsson, *Journal of Chemical Physics*, 2000, **113**, 9901-9904.
27. G. Henkelman and H. Jonsson, *The Journal of Chemical Physics*, 1999, **111**.
28. M. Vandichel, A. Moscu and H. Grönbeck, *ACS Catal.*, 2017, DOI: 10.1021/acscatal.7b02094, 7431-7441.
29. A. Ruiz Puigdollers, P. Schlexer, S. Tosoni and G. Pacchioni, *ACS Catal.*, 2017, **7**, 6493-6513.
30. G. Henkelman, A. Arnaldsson and H. Jónsson, *Computational Materials Science*, 2006, **36**, 354-360.
31. H. Michaelson, *Journal of Applied Physics*, 1977, **48**, 4729-4733.
32. F. Abild-Pedersen, J. Greeley, F. Studt, J. Rossmeisl, T. R. Munter, P. G. Moses, E. Skulason, T. Bligaard and J. K. Nørskov, *Phys Rev Lett*, 2007, **99**, 016105.
33. K. B. Srajan Kumar, T. N. Whittaker, C. Peterson, L. C. Grabow and B. D. Chandler, *J. Am. Chem. Soc.*, 2020, **142**, 5760-5772.
34. Q. Zhang, I. Lee, J. B. Joo, F. Zaera and Y. Yin, *Accounts Chem. Res.*, 2013, **46**, 1816-1824.